



Cite this: *Nanoscale Adv.*, 2022, 4, 4114

## Oxygen scavenging of HfZrO<sub>2</sub>-based capacitors for improving ferroelectric properties†

Bong Ho Kim,<sup>a</sup> Song-hyeon Kuk,<sup>a</sup> Seong Kwang Kim,<sup>a</sup> Joon Pyo Kim,<sup>a</sup> Dae-Myeong Geum,<sup>a</sup> Seung-Hyub Baek <sup>b</sup> and Sang Hyeon Kim <sup>\*,a</sup>

HfO<sub>2</sub>-based ferroelectric (FE) materials have emerged as a promising material for non-volatile memory applications because of remanent polarization, scalability of thickness below 10 nm, and compatibility with complementary metal–oxide–semiconductor technology. However, in the metal/FE/insulator/semiconductor, it is difficult to improve switching voltage ( $V_{sw}$ ), endurance, and retention properties due to the interfacial layer (IL), which inevitably grows during the fabrication. Here, we proposed and demonstrated oxygen scavenging to reduce the IL thickness in an HfZrO<sub>x</sub>-based capacitor and the thinner IL was confirmed by cross-sectional transmission electron microscopy.  $V_{sw}$  of a capacitor with scavenging decreased by 18% and the same  $P_r$  could be obtained at a lower voltage than a capacitor without scavenging. In addition, excellent endurance properties up to 10<sup>6</sup> cycles were achieved. We believe oxygen scavenging has great potential for future HfZrO<sub>x</sub>-based memory device applications.

Received 10th August 2022  
Accepted 13th August 2022

DOI: 10.1039/d2na00533f

rsc.li/nanoscale-advances

### Introduction

Since ferroelectricity was first reported in the early 1920s,<sup>1</sup> it was believed that the remanent polarization ( $P_r$ ) of ferroelectric (FE) materials even after the bias was removed would be used as the “0” and “1” states for non-volatile memory applications. In particular, an HfO<sub>2</sub>-based FE film has been spotlighted as a promising material for emerging memory devices because it is scalable without downgrading ferroelectricity even at a thickness below 10 nm and fully compatible with complementary metal–oxide–semiconductor technology.<sup>2</sup> Therefore, ferroelectricity of pure<sup>3–6</sup> and doped<sup>7–10</sup> HfO<sub>2</sub> has been extensively studied in the last few decades, and among them, laminated HfZrO<sub>x</sub> (HZO) has attracted much attention due to its lower crystallization temperature below 500 °C.<sup>11–15</sup>

However, when stacking FE films on Si substrates, the metal/FE/insulator/semiconductor (MFIS) structure is formed due to the native interfacial SiO<sub>x</sub> layer (IL) on the Si substrate. Even if the IL is removed in the pre-treatment step, the IL inevitably regrows due to the heat accompanied by the subsequent deposition and annealing process. On the other hand, the IL plays a critical role in the FE behavior, for example, inducing a large amount of charge trapping,<sup>16,17</sup> causing most of the voltage drop in the IL between the gate electrode and Si channel due to its lower dielectric constant (~3.9),<sup>18</sup> and destabilizing

the polarization state by forming a depolarization field.<sup>18,19</sup> As a result, the IL degrades overall performance metrics of FE-based devices such as  $P_r$ , switching voltage ( $V_{sw}$ ), endurance, and retention.<sup>20</sup> However, the existence of IL does not have only detrimental effects. The IL can reduce leakage current,<sup>21</sup> induce charge-assisted polarization,<sup>17,22</sup> and improve the crystallinity of the FE film.<sup>23</sup> These complex roles of the IL impose the difficulty of directly stacking FE films on Si substrates.<sup>24</sup> Although the inevitably formed IL is extremely challenging to deal with, it is important to control the MFIS structure for the FE film to be integrated into the gate stack of the field-effect-transistor (FET) with the channel region of the underlying Si. Ultimately, by engineering the IL, the FE film in the MFIS structure will be able to mitigate the aforementioned issues, resulting in significant improvement of the performance metrics.

On the other hand, the HZO thickness scaling directly leads to a reduction in  $V_{sw}$ , and improvement of endurance properties due to reduced voltage that reduces the energy of flowing electrons and the damage to HZO without IL thickness scaling, but the decrease in HZO thickness shows a fundamental trade-off of an increase in annealing temperature and a decrease in ferroelectric phase stability.<sup>25</sup> In addition, as the HZO thickness decreases,  $P_r$  decreases because domain wall switching becomes difficult due to the smaller grain size.<sup>26</sup> Therefore, IL engineering without loss in  $P_r$  and stability is required for one of the promising engineering directions. First, the insertion of an additional IL improved  $P_r$  and the endurance properties but not  $V_{sw}$ .<sup>27</sup> In contrast, reducing the IL thickness using microwave annealing that provides a lower thermal budget than conventional rapid thermal annealing (RTA) lowered  $V_{sw}$  but did not effectively inhibit IL formation during annealing, and the  $P_r$  was

<sup>a</sup>School of Electrical Engineering, Korea Advanced Institute of Science and Technology (KAIST), 34141 Daejeon, Republic of Korea. E-mail: shkim.ee@kaist.ac.kr

<sup>b</sup>Electronic Materials Research Center, Korea Institute of Science and Technology (KIST), 02792 Seoul, Republic of Korea

† Electronic supplementary information (ESI) available. See <https://doi.org/10.1039/d2na00533f>



less than  $5 \mu\text{C cm}^{-2}$ .<sup>28,29</sup> Alternatively, the improvement of endurance and retention properties by intentionally forming high- $k$  IL of SiON instead of SiO<sub>2</sub> using a high-temperature nitridation<sup>30,31</sup> and by using an epitaxial SiGe substrate that forms less IL compared to the Si substrate<sup>32</sup> has been reported. Moreover, oxygen scavenging, examined in high- $k$ /metal gate technology to reduce or eliminate IL, was conducted for IL scaling in the MFM structure,<sup>33,34</sup> MFIS structure,<sup>35</sup> and template layer,<sup>36</sup> but the effect on endurance and retention properties of MFIS structure is still unclear.

In this paper, we demonstrated the successful remote oxygen scavenging of HZO-based capacitors, highlighting the significant enhancement of FE properties. We fabricated capacitors of Au/TiN/HZO/Si (without scavenging) and Au/Ti/TiN/HZO/Si (with scavenging) stack and achieved successful IL thickness reduction by remote oxygen scavenging using Ti metal without increasing the process temperature, which was manifested by cross-section transmission electron microscopy (TEM). The capacitor with scavenging exhibited much lower  $V_{\text{sw}}$  and higher  $P_r$  at the same pulse amplitude than the control capacitor without scavenging. Furthermore, the capacitor with scavenging showed improved endurance properties, exhibiting  $P_r$  higher than  $10 \mu\text{C cm}^{-2}$  without breakdown up to  $10^6$  cycles at a pulse amplitude of 4 V and frequency of 10 kHz (4 V/10 kHz), while the capacitor without scavenging exhibited  $P_r$  higher than  $10 \mu\text{C cm}^{-2}$  up to only  $10^3$  cycles. The retention properties of the capacitor with scavenging were superior to those of the capacitor without scavenging, and 10 year retention was also verified by extrapolation. We believe that oxygen scavenging is a potential technique for FE devices with low  $V_{\text{sw}}$ , high  $P_r$ , and excellent endurance and retention properties.

## Experimental

### Fabrication of capacitors

For HZO-based capacitors, HZO films (10 nm) were deposited by thermal atomic layer deposition (ALD) on highly doped  $n$ -Si wafers that were pre-treated with buffered oxide etchant (BOE). Tetrakis(ethylmethylamino) hafnium (TEMAHf) and tetrakis(ethylmethylamino) zirconium (TEMAZr) were used as precursors and ozone was injected as the oxidant. For all ALD processes, the deposition temperature was maintained at 270 °C. Then, top electrodes of Au (100 nm)/TiN (20 nm) and Au (80 nm)/Ti (20 nm)/TiN (20 nm) were formed. To induce crystallization and oxygen scavenging, post-metallization annealing (PMA) was carried out by rapid thermal annealing (RTA) for 1 minute at 400, 500, and 600 °C in an N<sub>2</sub> atmosphere of 1 torr. The fabrication flow is depicted in Fig. 1c.

### Characterization of films

Cross-sectional view images of HZO-based capacitors were obtained by transmission electron microscopy (TEM; JEOL, JEM-ARM200F), with an accelerating voltage of 200 kV. The structural analysis of the phase and chemical bonding state of HZO films was performed by grazing incidence X-ray diffraction

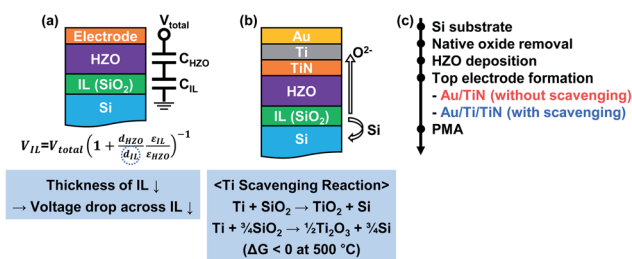


Fig. 1 (a) Schematic concept of the voltage drops across HZO and the IL in the MFIS structure. As the thickness of the IL decreases, the voltage drop across the IL decreases, which indicates that the IL thickness reduction can decrease  $V_{\text{sw}}$ . (b) Possible oxidation reaction of Ti in the MFIS structure. Negative Gibbs free energy suggests that oxygen scavenging is thermodynamically favored. (c) Fabrication flow of capacitors without and with scavenging. Ti metal was used as the oxygen scavenging metal.

(GIXRD; Rigaku, SmartLab) and X-ray photoelectron spectroscopy (XPS; ThermoFisher Scientific, K-Alpha+).

Electrical properties of devices were measured by using a parameter analyzer (Keithley, 4200A-SCS) with a pulse measurement unit (Keithley, 4225-PMU) and remote preamplifier/switch modules (Keithley, 4225-RPM). Pulse measurement schemes are presented in Fig. S2.† Fig. S2a† shows a typical polarization-voltage ( $P$ - $V$ ) hysteresis measurement using a bipolar triangular pulse and was used for switching voltage ( $V_{\text{sw}}$ ) extraction. Fig. S2b† shows a positive-up-negative-down (PUND) method using double pulses, which separates polarization and capacitive charging by subtracting the current measured in the first pulse (P and N) and the second pulse (U and D). Endurance and retention tests were performed as shown in Fig. S2c and d.†

## Results and discussion

### Fabrication of HZO-based capacitors via oxygen scavenging

Fig. 1a presents the schematic image of the typical MFIS capacitors with HZO and Si with an equivalent circuit of series capacitors with the SiO<sub>x</sub> IL. Here, the voltage across the IL and HZO is distributed depending on the relative thicknesses and dielectric constants of the IL and HZO. The trend of voltage drop distribution between the IL and HZO according to the IL thickness ( $d_{\text{IL}}$ ) is plotted in Fig. S1a† based on the typical dielectric constants of 3.9 and 30,<sup>37</sup> respectively. When the thickness of HZO ( $d_{\text{HZO}}$ ) is constant, a decrease in  $d_{\text{IL}}$  leads to an increase in capacitance of the IL, thus, the voltage drop across the IL ( $V_{\text{IL}}$ ) will be decreased. Therefore, a reduction in  $d_{\text{IL}}$  will promote FE switching by dominant voltage distribution across the HZO film. In addition, as shown in Fig. S1b,† the electric field across the IL is the same regardless of  $d_{\text{IL}}$ , so there is no concern about severe electric field across the IL.

Therefore, to ultimately reduce the IL at the interface between HZO and Si, we explored remote scavenging using Ti based on the reaction shown in Fig. 1b. Since Ti is thermodynamically favored to decompose SiO<sub>2</sub> considering Gibbs free energy (Fig. 1b),<sup>38</sup> we aimed remote oxygen scavenging by



introducing Ti on a thin TiN electrode in the gate stack. TiN was used as a barrier layer to prevent Ti diffusion, the intermixing between Ti and HZO, and the capping effect to obtain the ferroelectric orthorhombic phase. Au was used as a capping layer to prevent external oxygen penetration during PMA from the atmosphere. To investigate the effect of oxygen scavenging, we fabricated Au/TiN/HZO/Si (without scavenging) and Au/Ti/TiN/HZO/Si (with scavenging) capacitors following the fabrication flow depicted in Fig. 1c and details are in the Experimental section. As shown in cross-sectional TEM images of Fig. 2a–c, we successfully reduced  $d_{\text{IL}}$  without process temperature increase by oxygen scavenging with Ti metal. The  $d_{\text{IL}}$  of the as-deposited capacitor was 0.7 nm despite removal by the buffered oxide etchant in the pre-treatment. Then, after PMA, the  $d_{\text{IL}}$  increased to 1 nm in the capacitor without scavenging and remarkably decreased to 0.3 nm in the capacitor with scavenging, indicating that the IL re-grew and was scavenged by PMA, respectively. Consequently, according to the voltage drop distribution in Fig. S1a,† in the capacitor without scavenging, a voltage of 43% and 57% will be applied to the IL and HZO, respectively. In the capacitor with scavenging, the  $V_{\text{IL}}$  will be reduced to 19%.

Meanwhile, the fast Fourier transform images shown in the insets of Fig. 2a–c reveal that PMA induced not only oxygen

scavenging but also crystallization from the amorphous structure to poly-crystalline orthorhombic phase. The interplanar distance of 0.307 nm also matches well with the o(111) plane.<sup>39</sup> For further structural analysis of HZO after PMA, GIXRD and XPS were performed. As shown in Fig. 2d, GIXRD peaks appeared at 30.8 and 35.5° only in w/o scavenging and scavenged HZO, implying that the amorphous structure of as-deposited HZO was transformed into a mixture of orthorhombic and tetragonal phases after PMA.<sup>40</sup> In the XPS spectra of Hf 4f and Zr 3d binding energy levels shown in Fig. 2e, the Hf 4f<sub>7/2</sub> and Zr 3d<sub>5/2</sub> peaks appeared at 17.7 and 183.1 eV with peak differences of 1.71 and 2.43 eV, respectively, as previously reported in HZO films.<sup>41</sup> Note that TEM, GIXRD, and XPS analyses showed no significant structural differences between the HZO film w/o scavenging and with scavenging. This is because HZO films are dominantly affected by the tensile stress induced by the top and bottom electrodes, in particular, the latter,<sup>42</sup> but both electrodes of our HZO films were the same as TiN and highly doped *n*-Si. Therefore, it can be considered that the difference in electrical and FE properties to be discovered in device measurement in the following section mainly originates from the difference in the  $d_{\text{IL}}$ .

### Effect of oxygen scavenging on ferroelectricity of HZO-based capacitors

Detailed pulse measurement methods are depicted in the Experimental section and Fig. S2.† Based on  $P_r$ ,  $V_{\text{sw}}$ , and leakage characteristics in the transient current ( $I$ - $V$ ) curves during the polarization switching and the polarization-voltage ( $P$ - $V$ ) hysteresis curves shown in Fig. S3 and S4,† the PMA temperature was optimized at 500 °C since PMA at 400 and 600 °C induced oxygen scavenging insufficiently and excessively, thus, the  $V_{\text{sw}}$  decreased slightly in the former and in the latter, the leakage increased significantly. Fig. 3a shows the results of the positive-up-negative-down (PUND) measurement of both

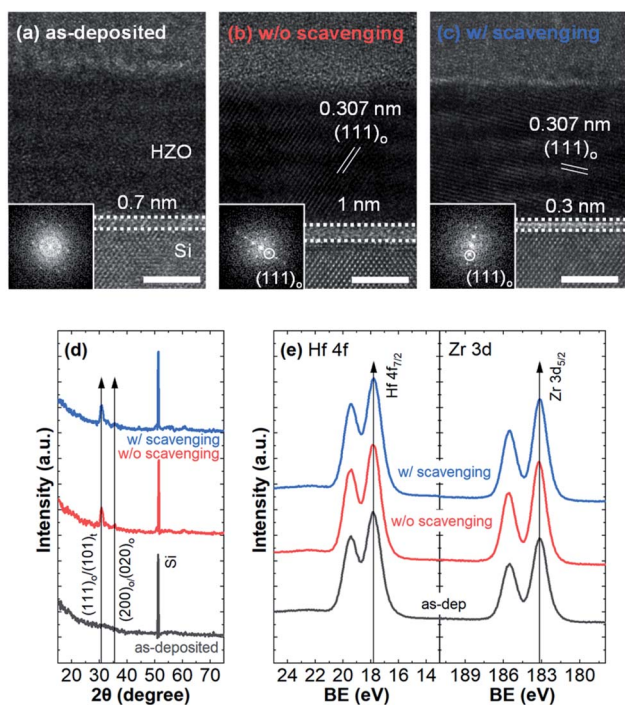


Fig. 2 (a)–(c) Cross-sectional TEM images of as-deposited capacitors and capacitors without and with scavenging (all scale bars are 4 nm). After PMA, regrowth and scavenging of IL were observed in capacitors without and with scavenging, respectively. HZO crystallization was also confirmed in both capacitors. (d) GIXRD and (e) XPS results of as-deposited HZO and HZO without and with scavenging. The diffraction peaks of GIXRD show crystallization of HZO by PMA. Meanwhile, GIXRD and XPS results show no structural difference between HZO without and with scavenging.

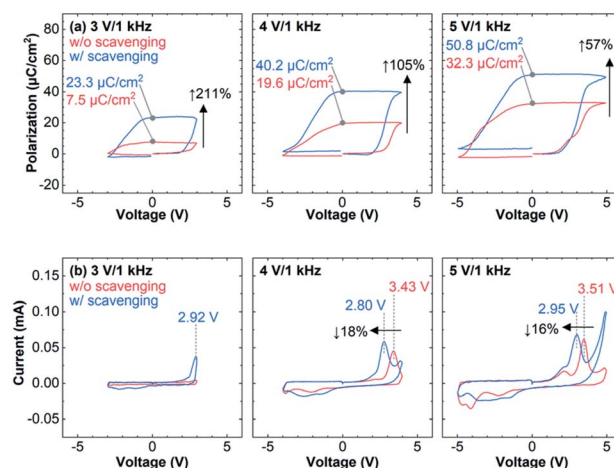


Fig. 3 (a)  $P$ - $V$  curves by the PUND method. (b)  $I$ - $V$  curves using a bipolar triangular pulse. The  $V_{\text{sw}}$  of the capacitor with scavenging was lower than that of the capacitor without scavenging. Due to the lower  $V_{\text{sw}}$ , the  $P_r$  of the capacitor with scavenging was higher than that of the capacitor without scavenging at the same pulse amplitudes.





capacitors, which can compensate for leakage and capacitive charging of FE by double triangular pulses (Fig. S2a†). Since the MFIS structure is asymmetric in structure and carrier response,<sup>17,43</sup> the  $P$ - $V$  curves are not centered and are displayed as measured. The capacitor with scavenging exhibited higher  $P_r$  than the capacitor without scavenging at the same pulse due to the lower  $V_{sw}$  resulting from the thinner IL. At a pulse of 4 V/1 kHz and 5 V/1 kHz,  $P_r$  of the capacitor with scavenging increased by 105 and 57% than that of the capacitor without scavenging, respectively. In particular, at a pulse of 3 V/1 kHz,  $P_r$  increased by 211%, indicating that a 3 V/1 kHz pulse can induce ferroelectric switching in the capacitor with scavenging but is insufficient in the capacitor without scavenging.

Fig. 3b,  $I$ - $V$  curves of capacitors without and with scavenging with the bipolar triangular pulse to the gate (Fig. S2b†), shows  $V_{sw}$  clearly. At a pulse of 4 V/1 kHz, capacitors without and with scavenging exhibited  $V_{sw}$  of 3.43 and 2.80 V, respectively, which means that  $V_{sw}$  was reduced by 16% by oxygen scavenging. According to the voltage drop distribution,  $V_{HZO}$  at  $V_{sw}$  of capacitors without and with scavenging is 2.35 and 2.09 V, which is about 12% different. This is because the voltage drop distribution dominates the ferroelectric switching behavior but other factors such as charge-assisted polarization also play a role.<sup>22</sup> Therefore, the  $E_{TL}$  of the capacitor with scavenging at  $V_{sw}$ , which was the same as that of the capacitor without scavenging when only the voltage drop distribution is considered in Fig. S1b,† will be slightly higher than that of the capacitor without scavenging. But since the charge-assisted polarization is less in the capacitor with scavenging, the damage caused by trapping will be also less, and further measurements are required to compare reliability properties. The leakage characteristics of the capacitor with scavenging shown in  $I$ - $V$  curves (Fig. 3b) will also affect the reliability. In other words, as the IL became thinner by oxygen scavenging,  $V_{sw}$  and charge trapping decreased while  $E_{TL}$  and leakage increased. Nevertheless, it should be noted that the capacitor with scavenging can exhibit the same  $P_r$  as the capacitor without scavenging at a lower pulse amplitude, which can compensate the increased  $E_{TL}$  and leakage.

In order to investigate the effect of oxygen scavenging on the reliability of HZO-based capacitors, the endurance test was carried out (Fig. S2c†). Bipolar triangular pulses with an amplitude of 3 to 6 V and a frequency of 1 to 100 kHz were applied, and  $P_r$  extracted from the PUND method and endurance properties of capacitors without and with scavenging were mapped in Fig. 4. Fig. 4a and b mapped the  $P_r$  of capacitors without and with scavenging, but only  $P_r$  over  $10 \mu\text{C cm}^{-2}$  (minimum  $P_r$  for MW to saturate in the FEFET)<sup>43</sup> was displayed in color. Attributed to the much reduced  $V_{sw}$  of the capacitor with scavenging, the  $P_r$  map of the capacitor with scavenging shifted to a lower voltage than that of the capacitor without scavenging. Additionally, in both capacitors, higher amplitudes were required to obtain the same level of  $P_r$  at higher frequencies. On the endurance map in Fig. 4c-f, boundaries indicating initial  $P_r$  of 10 and  $30 \mu\text{C cm}^{-2}$  derived from Fig. 4a and b were overlaid by black and white dashed lines, respectively. First, Fig. 4c and d are maps of the endurance cycles until breakdown occurred. The regions where breakdown did not occur until  $10^6$

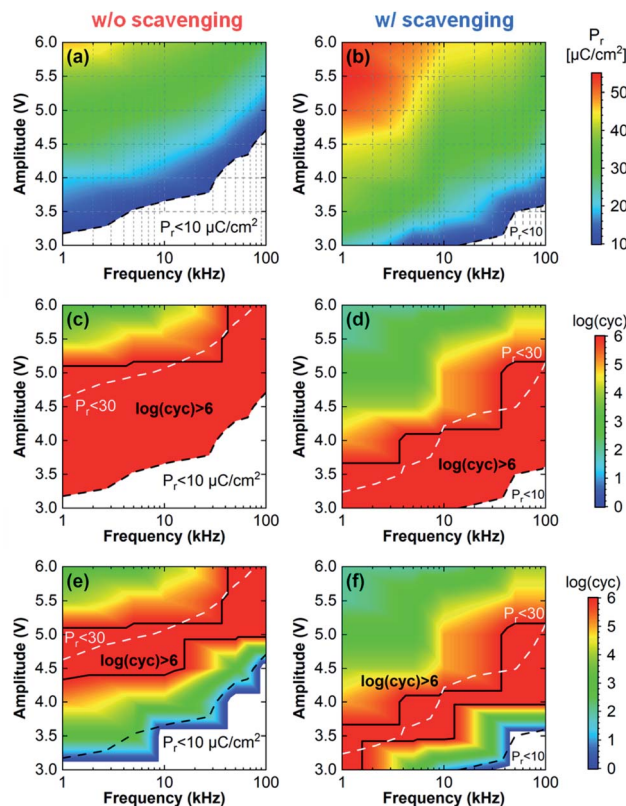


Fig. 4 Maps of  $P_r$  extracted from the PUND method of capacitors (a) without scavenging and (b) with scavenging. Endurance maps until (c), (d) breakdown occurred and (e), (f)  $P_r$  reached  $10 \mu\text{C cm}^{-2}$ . The black and white dashed lines indicate  $P_r$  of 10 and  $30 \mu\text{C cm}^{-2}$ , respectively. The black solid line indicates the region with endurance cycles higher than  $10^6$ .

cycles were marked by black solid lines. Note that although only  $10^6$  cycles are displayed for visibility of maps, breakdown did not occur until  $10^9$  cycles for the capacitors without and with scavenging at the pulses of 4.5 V/100 kHz and 3.5 V/100 kHz, respectively. Interestingly, this region tended to occur at initial  $P_r$  below  $30 \mu\text{C cm}^{-2}$ . For a multifaceted analysis of endurance properties, the endurance cycles until  $P_r$  reached  $10 \mu\text{C cm}^{-2}$  were mapped in Fig. 4e and f because in device operation, maintaining  $P_r$  effectively is as important as breakdown not occurring. The regions in which  $P_r$  was maintained over  $10 \mu\text{C cm}^{-2}$  until  $10^6$  cycles were also marked by black solid lines, and the regions spanned the lines with an initial  $P_r$  of  $30 \mu\text{C cm}^{-2}$ . Analysis of  $P_r$  and endurance maps showed that both capacitors exhibited high endurance properties, maintaining  $P_r$  over  $10 \mu\text{C cm}^{-2}$  without breakdown until  $10^6$  cycles at moderate pulses. Otherwise, in specific pulses, the capacitor with scavenging showed superior endurance properties to the capacitor without scavenging due to the lowered  $V_{sw}$ . For instance, at 3.5 V/10 kHz, where capacitors without scavenging did not exhibit an initial  $P_r$  exceeding  $10 \mu\text{C cm}^{-2}$ , the capacitors with scavenging maintained  $P_r$  over  $10 \mu\text{C cm}^{-2}$  until  $10^6$  cycles. At 4 V/10 kHz, capacitors without and with scavenging showed  $10^3$  and  $10^6$  cycles maintaining  $P_r$  over  $10 \mu\text{C cm}^{-2}$ . At 4.5 V/10 kHz, the capacitors without scavenging finally reached  $10^6$  cycles.



However, since both capacitors have different  $V_{sw}$ , we compare endurance properties based on the initial  $P_r$  rather than the applied pulse. The endurance properties until breakdown occurred and  $P_r$  decreased to  $10 \mu\text{C cm}^{-2}$  according to initial  $P_r$  are shown in Fig. S6.† In both capacitors, breakdown did not occur up to  $10^6$  cycles at initial  $P_r$  below  $30 \mu\text{C cm}^{-2}$  regardless of pulse frequency (Fig. S6a†). However, at lower initial  $P_r$ ,  $P_r$  reached  $10 \mu\text{C cm}^{-2}$  in earlier cycling (Fig. S6b†). The endurance measurement results according to initial  $P_r$  suggest that oxygen scavenging can effectively lower the  $V_{sw}$  while maintaining  $P_r$  without deteriorating the endurance properties of the HZO-based capacitors.

The endurance test proved that the endurance properties of the capacitor with scavenging were comparable to or even better than those of the capacitor without scavenging. As mentioned above, this is because  $V_{sw}$  and charge trapping decreased despite the increase in  $E_{IL}$  and leakage by oxygen scavenging. Analysis of initial internal fields ( $E_{int}$ ) and XPS can verify decreased charge trapping in the capacitor with scavenging. Referring to the imprint effect of the  $P$ - $V$  curves in Fig. S7,† the  $E_{int}$  of the capacitors without and with scavenging was  $0.277$  and  $0.385 \text{ MV cm}^{-1}$ , respectively, at a pulse of  $6 \text{ V}/10 \text{ kHz}$ . The  $E_{int}$  can be readily calculated as the average of positive and negative  $V_{sw}$ . Since the direction of  $E_{int}$  is opposite to that of the  $P$ - $V$  curve shift, the negative shift of the  $P$ - $V$  curve is consistent with the direction of  $E_{int}$  from the top electrode to the bottom electrode. The  $E_{int}$  is formed inside the FE materials by the difference in the work function between the top electrode and the bottom electrode,<sup>44</sup> the difference in the areal density of oxygen atoms at the interfacial oxide,<sup>45</sup> and the asymmetric distribution of oxygen vacancies at the interface.<sup>46</sup> However, in our capacitors without and with scavenging, the top electrode and the bottom electrode are the same as TiN and high-doped  $n$ -Si and the IL is also the same as  $\text{SiO}_2$ . Thus, it seems that the differences in oxygen vacancy distribution at the top and bottom interfaces of both capacitors lead to different  $E_{int}$ . The sub-oxide peaks of the deconvoluted XPS Hf 4f spectra in Fig. S8† reveal that the existence of oxygen vacancies at the top interface and its density are similar in both capacitors. The fact that the initial  $E_{int}$  of the capacitor with scavenging was higher than that of the capacitor without scavenging suggests that the density of positively charged oxygen vacancies at the bottom interface of the capacitor with scavenging would be less than that of the capacitor without scavenging, which is consistent with the interpretation of charge-assisted polarization in Fig. 3b. The existence of oxygen vacancies at the top interface is because TiN of the top electrode generates oxygen vacancies at the top interface of HZO during the TiN deposition process and PMA.<sup>42</sup> On the other hand, as shown in Fig. S7,† the  $E_{int}$  of capacitors without and with scavenging negatively shifted to  $-1.155$  and  $-0.479 \text{ MV cm}^{-1}$ , respectively, after endurance tests of  $10^3$  and  $10^2$  cycles at  $6 \text{ V}/10 \text{ kHz}$ , which means that oxygen vacancies are drastically generated at the bottom interface during cycling. This negative imprint shift indicates the endurance issue due to IL degradation caused by charge trapping in the IL of the MFIS structure.<sup>47</sup> In addition, despite the oxygen vacancy distribution differing by 15% between pristine capacitors without and with scavenging, the wake-up and fatigue, a gradual increase and

decrease in  $P_r$  with cycling, which is a typical phenomenon in ferroelectric HZO, were similar to that shown in Fig. S5.† Since wake-up and fatigue are closely related to domain pinning/depinning and oxygen vacancy redistribution,<sup>48</sup> it is suggested that these phenomena are not significantly different between capacitors without and with scavenging. It was found that oxygen scavenging adversely affected not only endurance properties but also wake-up and fatigue, which are undesirable for the reliability of long-term device operation.

Finally, the retention of  $P_r$  was measured for positive and negative poling voltages at room temperature for low-temperature characterization and presented in Fig. 5. The data that were measured by pulses ( $5 \text{ V}/10 \text{ kHz}$  and  $6 \text{ V}/100 \text{ kHz}$  for capacitors without scavenging and  $4 \text{ V}/10 \text{ kHz}$  and  $5 \text{ V}/100 \text{ kHz}$  for capacitors with scavenging) with similar initial  $P_r$  while exhibiting endurance properties of higher than  $10^6$  cycles in both capacitors were extrapolated up to 10 years. In positive poling with  $5 \text{ V}/10 \text{ kHz}$  and  $4 \text{ V}/10 \text{ kHz}$  pulses, the retention

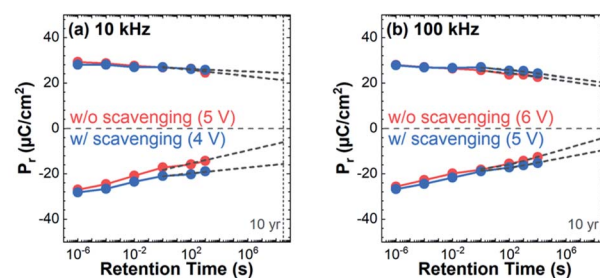


Fig. 5 Retention properties of capacitors without scavenging and with scavenging at pulses (a) 10 kHz and (b) 100 kHz) with similar initial  $P_r$  and exhibiting endurance properties of higher than  $10^6$  cycles. 10 year retention properties for both capacitors were expected from the extrapolation.

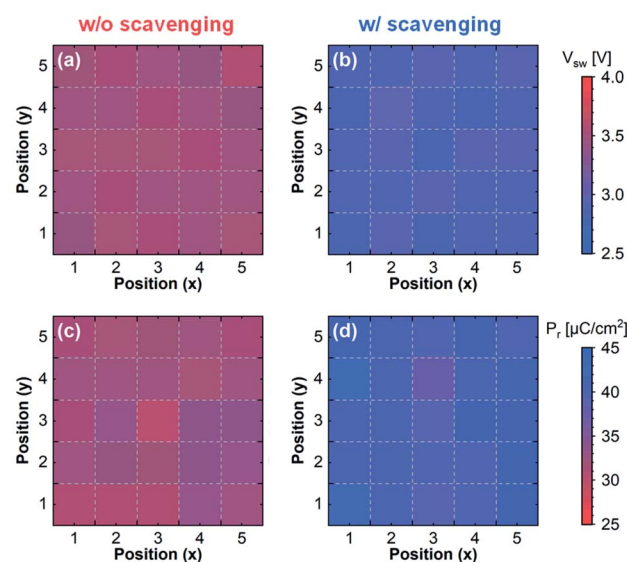


Fig. 6 Uniformity maps of (a), (b)  $V_{sw}$  and (c), (d)  $P_r$  of capacitors without and with scavenging. 25 capacitors for each were measured in an area of  $1 \times 1 \text{ cm}^2$ .



Table 1 Benchmark of our MFIS capacitors without and with scavenging with other reported studies

	This work		49	50	51	32	52	53
	With scavenging	Without scavenging						
Ferroelectric oxide (thickness [nm])	HZO (10)	HZO (10)	Al:HfO <sub>2</sub> (20)	HZO (20)	HfO <sub>2</sub> (10)	HZO (10)	HZO (13)	HZO (10)
PMA temperature [°C]	500	500	900	600	N/A	500	750	700
Pulse amplitude [V]	4	4	10	6	3	4	4	2
Pulse frequency [kHz]	10	10	N/A	N/A	N/A	1	1	N/A
$P_r$ [ $\mu\text{C cm}^{-2}$ ]	28	16	40	25	8	35	45	N/A
Endurance until breakdown [cycles]	$>10^6$	$>10^6$	$>10^4$	$>10^5$	$10^5$	$10^6$	$10^3$	$>10^7$
Endurance until $P_r > 10 \mu\text{C cm}^{-2}$ [cycles]	$>10^6$	$>10^3$	$>10^4$	$>10^5$	0	$10^6$	$10^3$	N/A

properties at 10 years of both capacitors were stable, with  $P_r$  exceeding  $20 \mu\text{C cm}^{-2}$  and maintaining 73 and 87% in capacitors without and with scavenging, respectively. In contrast, retention was not only relatively unstable in negative poling, but there was also a large gap between capacitors without and with scavenging. The  $P_r$  of capacitors without scavenging decreased to 22 and 17% and was less than  $10 \mu\text{C cm}^{-2}$  at 10 year retention extrapolation in negative poling with 5 V/10 kHz and 6 V/100 kHz pulses while capacitors with scavenging showed  $P_r$  over  $10 \mu\text{C cm}^{-2}$  and kept it at 55 and 37% at 4 V/10 kHz and 5 V/100 kHz. The unstable retention characteristics in negative poling are due to electron trapping that occurs in positive pulses. In the typical MFIS structure, the behavior of electrons and holes is asymmetric. As a large amount of electrons ( $\sim 10^{14} \text{ cm}^{-2}$ )<sup>43</sup> trapped in positive pulses are gradually detrapped according to the retention time,<sup>17</sup> the retention characteristics of  $P_r$  become unstable. Therefore, the superior retention characteristics of capacitors with scavenging over capacitors without scavenging are attributed to the lower depolarization field<sup>54</sup> and less charge trapping owing to the thinner IL.

### Potential of oxygen scavenging in HZO-based devices

Uniformity was acquired to validate the potential of oxygen scavenging for industrial applications. The spatial distribution maps of  $V_{sw}$  and  $P_r$  of 25 capacitors without and with scavenging in an area of  $1 \times 1 \text{ cm}^2$  are displayed in Fig. 6. Pulses of 5 V/1 kHz and 4 V/1 kHz were applied to capacitors without and with scavenging. Fig. 6a and b present that the average  $V_{sw}$  of capacitors without and with scavenging was 3.48 and 2.91 V with very small standard deviations of 0.038 V and 0.034 V, respectively. The average  $P_r$  extracted from the PUND method of capacitors without and with scavenging was 32.1 and  $40.3 \mu\text{C cm}^{-2}$  with standard deviations of 1.01 and  $1.13 \mu\text{C cm}^{-2}$ , respectively (Fig. 6c and d). In Fig. S9,† the detailed  $V_{sw}$  and  $P_r$  of 25 capacitors without and with scavenging are shown. The excellent uniformity and high yield of capacitors with scavenging confirmed by quantitative results indicate that oxygen scavenging does not impair uniformity and is suitable for large-area fabrication.

Furthermore, the benchmark in Table 1 highlights the low-voltage operation and high endurance properties of our capacitors with scavenging. In the MFIS structure, we achieved a high  $P_r$  of  $28 \mu\text{C cm}^{-2}$  and endurance properties of  $>10^6$  cycles

maintaining  $P_r$  higher than  $10 \mu\text{C cm}^{-2}$  at a pulse of 4 V/10 kHz with annealing at a low temperature of 500 °C *via* oxygen scavenging. The capacitor with scavenging showed outstanding performances compared to the capacitor without scavenging as well as other previous MFIS structures.<sup>32,49–53</sup>

## Conclusions

We demonstrated oxygen scavenging by introducing Ti metal in the top electrode stack to improve the performance of HZO-based devices. The reduction in IL thickness *via* oxygen scavenging was manifested by TEM cross-sectional images, and no structural difference between w/o scavenging and scavenged HZO films was observed in XRD and XPS analyses. The capacitors with scavenging exhibited low-voltage operation and excellent endurance and retention properties. The  $V_{sw}$  was decreased by 18%, from 3.43 V to 2.80 V for capacitors without and with scavenging, respectively. Due to the lower  $V_{sw}$ , the same  $P_r$  could be obtained at a lower voltage than the capacitor without scavenging. In addition, the capacitor with scavenging showed endurance properties exceeding  $10^6$  cycles while maintaining  $P_r$  higher than  $10 \mu\text{C cm}^{-2}$  without breakdown, which was superior to the capacitor without scavenging showing  $10^3$  cycles. 10 year retention and uniformity were also confirmed. Finally, we believe that oxygen scavenging has great potential to improve the FE properties of HZO-based devices.

## Conflicts of interest

There are no conflicts to declare.

## Acknowledgements

This work was supported by the NRF grant (No. 2019M3F3A1A02072072 and 2020M3F3A2A01110575), BK21 FOUR, KAIST for PIM (N11220038), and the IC Design Education Center.

## References

- 1 J. Valasek, *Phys. Rev.*, 1921, **17**, 475.
- 2 J. Müller, T. Böscke, D. Bräuhäus, U. Schröder, U. Böttger, J. Sundqvist, P. Kücher, T. Mikolajick and L. Frey, *Appl. Phys. Lett.*, 2011, **99**, 112901.





- 3 P. Polakowski and J. Müller, *Appl. Phys. Lett.*, 2015, **106**, 232905.
- 4 K. Kim, M. Park, H. Kim, Y. Kim, T. Moon, Y. Lee, S. Hyun, T. Gwon and C. Hwang, *J. Mater. Chem. C*, 2016, **4**, 6864–6872.
- 5 A. Pal, V. K. Narasimhan, S. Weeks, K. Littau, D. Pramanik and T. Chiang, *Appl. Phys. Lett.*, 2017, **110**, 022903.
- 6 H. Chen, Y. Chen, L. Tang, H. Luo, K. Zhou, X. Yuan and D. Zhang, *J. Mater. Chem. C*, 2020, **8**, 2820–2826.
- 7 K. Lee, T. Y. Lee, S. M. Yang, D. H. Lee, J. Park and S. C. Chae, *Appl. Phys. Lett.*, 2018, **112**, 202901.
- 8 S. Vulpe, F. Nastase, M. Dragoman, A. Dinescu, C. Romanitan, S. Iftimie, A. Moldovan and N. Apostol, *Appl. Surf. Sci.*, 2019, **483**, 324–333.
- 9 H. Mulaosmanovic, E. T. Breyer, T. Mikolajick and S. Slesazeck, *IEEE Trans. Electron Devices*, 2019, **66**, 3828–3833.
- 10 F. Mehmood, M. Hoffmann, P. D. Lomenzo, C. Richter, M. Materano, T. Mikolajick and U. Schroeder, *Adv. Mater. Interfaces*, 2019, **6**, 1901180.
- 11 M. H. Park, H. J. Kim, Y. J. Kim, W. Lee, T. Moon and C. S. Hwang, *Appl. Phys. Lett.*, 2013, **102**, 242905.
- 12 S. Zarubin, E. Suvorova, M. Spiridonov, D. Negrov, A. Chernikova, A. Markeev and A. Zenkevich, *Appl. Phys. Lett.*, 2016, **109**, 192903.
- 13 M. H. Park, Y. H. Lee, H. J. Kim, T. Schenk, W. Lee, K. Do Kim, F. P. Fengler, T. Mikolajick, U. Schroeder and C. S. Hwang, *Nanoscale*, 2017, **9**, 9973–9986.
- 14 M. G. Kozodaev, A. G. Chernikova, E. V. Korostylev, M. H. Park, R. R. Khakimov, C. S. Hwang and A. M. Markeev, *J. Appl. Phys.*, 2019, **125**, 034101.
- 15 S. L. Weeks, A. Pal, V. K. Narasimhan, K. A. Littau and T. Chiang, *ACS Appl. Mater. Interfaces*, 2017, **9**, 13440–13447.
- 16 K. Toprasertpong, M. Takenaka, and S. Takagi in *2019 IEEE International Electron Devices Meeting (IEDM)*, 2019, pp. 23.27.21–23.27.24.
- 17 S.-H. Kuk, S.-M. Han, B.-H. Kim, S.-H. Baek, J.-H. Han, and S.-H. Kim in *2021 IEEE International Electron Devices Meeting (IEDM)*, 2021, pp. 33.36.31–33.36.34.
- 18 K. Ni, P. Sharma, J. Zhang, M. Jerry, J. A. Smith, K. Tapily, R. Clark, S. Mahapatra and S. Datta, *IEEE Trans. Electron Devices*, 2018, **65**, 2461–2469.
- 19 D. Zhao, T. Lenz, G. H. Gelinck, P. Groen, D. Damjanovic, D. M. de Leeuw and I. Katsouras, *Nat. Commun.*, 2019, **10**, 1–11.
- 20 J. Lyu, I. Fina and F. Sanchez, *Appl. Phys. Lett.*, 2020, **117**, 072901.
- 21 K. K. Min, J. Yu, Y. Kim, J.-H. Lee, D. Kwon and B.-G. Park, *Nanotechnology*, 2021, **32**, 495203.
- 22 T. Kim and C. Shin, *Electronics*, 2020, **9**, 2141.
- 23 W. Xiao, C. Liu, Y. Peng, S. Zheng, Q. Feng, C. Zhang, J. Zhang, Y. Hao, M. Liao and Y. Zhou, *IEEE Electron Device Lett.*, 2019, **40**, 714–717.
- 24 M. H. Park, Y. H. Lee, H. J. Kim, Y. J. Kim, T. Moon, K. D. Kim, J. Mueller, A. Kersch, U. Schroeder and T. Mikolajick, *Adv. Mater.*, 2015, **27**, 1811–1831.
- 25 K. Tahara, K. Toprasertpong, Y. Hikosaka, K. Nakamura, H. Saito, M. Takenaka, and S. Takagi in *2021 IEEE Symposium on VLSI Technology*, 2021, p. 1.
- 26 S. J. Kim, J. Mohan, J. Lee, J. S. Lee, A. T. Lucero, C. D. Young, L. Colombo, S. R. Summerfelt, T. San and J. Kim, *Appl. Phys. Lett.*, 2018, **112**, 172902.
- 27 W. Xiao, C. Liu, Y. Peng, S. Zheng, Q. Feng, C. Zhang, J. Zhang, Y. Hao, M. Liao and Y. Zhou, *Nanoscale Res. Lett.*, 2019, **14**, 1–7.
- 28 Y.-H. Chen, C.-J. Su, C. Hu and T.-L. Wu, *IEEE Electron Device Lett.*, 2019, **40**, 467–470.
- 29 Y.-H. Chen, C.-J. Su, T.-H. Yang, C. Hu and T.-L. Wu, *IEEE Trans. Electron Devices*, 2020, **67**, 1581–1585.
- 30 T. Ali, P. Polakowski, S. Riedel, T. Büttner, T. Kämpfe, M. Rudolph, B. Pätzold, K. Seidel, D. Löhr and R. Hoffmann, *IEEE Trans. Electron Devices*, 2018, **65**, 3769–3774.
- 31 A. J. Tan, Y.-H. Liao, L.-C. Wang, N. Shanker, J.-H. Bae, C. Hu and S. Salahuddin, *IEEE Electron Device Lett.*, 2021, **42**, 994–997.
- 32 K.-Y. Chen, Y.-H. Huang, R.-W. Kao, Y.-X. Lin, K.-Y. Hsieh and Y.-H. Wu, *IEEE Trans. Electron Devices*, 2019, **66**, 3636–3639.
- 33 Y. Goh, S. H. Cho, S.-H. K. Park and S. Jeon, *Nanoscale*, 2020, **12**, 9024–9031.
- 34 F. Zhang, Z.-D. Luo, Q. Yang, J. Zhou, J. Wang, Z. Zhang, Q. Fan, Y. Peng, Z. Wu and F. Liu, *ACS Appl. Mater. Interfaces*, 2022, **14**, 11028–11037.
- 35 Y. B. Lee, B. Y. Kim, H. W. Park, S. H. Lee, M. Oh, S. K. Ryoo, I. S. Lee, S. Byun, D. Shim and J. H. Lee, *Adv. Electron. Mater.*, 2022, 2200310.
- 36 S. Fujii, M. Yamaguchi, S. Kabuyanagi, K. Ota, and M. Saitoh in *2020 IEEE Symposium on VLSI Technology*, 2020, pp. 1–2.
- 37 T. Böske, P. Hung, P. Kirsch, M. Quevedo-Lopez and R. Ramírez-Bon, *Appl. Phys. Lett.*, 2009, **95**, 052904.
- 38 D. R. Lide, *CRC Handbook of Chemistry and Physics*, CRC Press, 2004.
- 39 T.-J. Chang, C. Liu, C.-C. Fan, H.-H. Hsu, H.-H. Chen, W.-H. Chen, Y.-C. Fan, T.-M. Lee, C.-L. Lin and J. Ma, *Vacuum*, 2019, **166**, 11–14.
- 40 S. H. Kim, G. T. Yu, G. H. Park, D. H. Lee, J. Y. Park, K. Yang, E. B. Lee, J. I. Lee and M. H. Park, *Chem. Commun.*, 2021, **57**, 12452–12455.
- 41 Y. Peng, G. Han, W. Xiao, Y. Liu, Q. Li, C. Zhang, J. Zhang and Y. Hao, *Superlattices Microstruct.*, 2019, **130**, 519–527.
- 42 Y. Lee, Y. Goh, J. Hwang, D. Das and S. Jeon, *IEEE Trans. Electron Devices*, 2021, **68**, 523–528.
- 43 K. Toprasertpong, Z. Lin, T. Lee, M. Takenaka, and S. Takagi in *2020 IEEE Symposium on VLSI Technology*, 2020, pp. 1–2.
- 44 F. Liu, I. Fina, R. Bertacco and J. Fontcuberta, *Sci. Rep.*, 2016, **6**, 1–7.
- 45 K. Kita and A. Toriumi, *Appl. Phys. Lett.*, 2009, **94**, 132902.
- 46 M. Park, H. Kim, Y. Kim, T. Moon, K. Kim, Y. Lee, S. Hyun and C. Hwang, *J. Mater. Chem. C*, 2015, **3**, 6291–6300.
- 47 N. Gong and T.-P. Ma, *IEEE Electron Device Lett.*, 2017, **39**, 15–18.



- 48 S. Li, D. Zhou, Z. Shi, M. Hoffmann, T. Mikolajick and U. Schroeder, *Adv. Electron. Mater.*, 2020, **6**, 2000264.
- 49 H. Ryu, K. Xu, J. Guo, and W. Zhu in *2018 76th Device Research Conference (DRC)*, 2018, pp. 1–2.
- 50 H. Ryu, K. Xu, D. Kim, F. Rao, and W. Zhu in *49th IEEE Semiconductor Interface Specialists Conference*, 2018.
- 51 Y.-T. Lee, H.-H. Chen, Y.-C. Tung, B.-Y. Shih, S.-Y. Hsiung, T.-M. Lee, C.-C. Hsu, C. Liu, H.-H. Hsu, and C.-Y. Chang in *2019 IEEE International Conference on Electron Devices and Solid-State Circuits (EDSSC)*, 2019, pp. 1–3.
- 52 C. Zacharaki, P. Tsipas, S. Chaitoglou, S. Fragkos, M. Axiotis, A. Lagoyiannis, R. Negrea, L. Pintilie and A. Dimoulas, *Appl. Phys. Lett.*, 2019, **114**, 112901.
- 53 H.-H. Hsu, H.-M. Liu and S. Lee, *Coatings*, 2020, **10**, 733.
- 54 M. Lederer, K. Mertens, A. M. Kia, J. Emara, R. Olivo, Y. Raffel, D. Lehninger, T. Ali, K. Kühnel and K. Seidel, *MRS Adv.*, 2021, **6**, 525–529.

